High temperature reflectometer for spatially resolved spectral directional emissivity of laser powder bed fusion processes

David C. Deisenroth[1,a], Leonard Hanssen[a], and Sergey Mekhontsev[b]
[a]National Institute of Standards and Technology, 100 Bureau Drive, Gaithersburg, MD 20899
[b]Jung Research and Development Corporation, 5508 Cromwell Drive, Bethesda, MD 20816

ABSTRACT

Additive manufacturing involving layer-wise selective laser melting of a powder material, or laser powder bed fusion (LPBF), is a fast-growing industry. At the Additive Manufacturing Metrology Testbed (AMMT) at the United States National Institute of Standards and Technology (NIST) an integrating hemispherical reflectometer has recently been developed to facilitate measurements of spatially resolved reflectance of the laser-melting heat affected zone (HAZ) during the LPBF process. Reflectance is then used to determine spatially resolved emissivity. The design features of the hemispherical-directional reflectometer are discussed. Then, the reflectometer performance and measurement uncertainties are detailed. A two-dimensional map of emissivity and emissivity uncertainty of the HAZ around a meltpool of high-purity nickel are presented. It is found that emissivity measurements are in good agreement with literature values at the melting point of high-purity nickel with acceptable uncertainty.

Keywords: High-temperature baffle-less reflectometer, emissivity of high-temperature metals, laser powder bed fusion

1. INTRODUCTION

Laser powder bed fusion (LPBF) is a layer-wise selective melting of the metal powder by scanning a high-power laser across the powder bed, which is located inside a process chamber with low oxygen content and laminar flow of protective gas. It is a fast-growing industry with unique fabrication capabilities compared to more traditional casting and forging [1]. Physical understanding of the processes taking place in laser-based additive manufacturing processes, such as LBPF and others, can be significantly enhanced by the knowledge of the thermodynamic surface temperature distribution [2]. The utility of thermodynamic surface temperature distribution includes, but is not limited to, the study of the rapid solidification of molten metal, which defines the metallographic structure—and associated mechanical properties—of the resulting part.

To establish traceable radiance-based temperature measurements we have selected the only first principle approach which is applicable, (1) direct measurement of spectral radiance of the heat-affected zone (HAZ) by comparison with a radiance standard, (2) indirect measurement of spectral emissivity, by illuminating the sample with a uniform hemispherical source and comparing the reflected radiant flux to that from a calibrated standard, and (3) calculation of the surface temperature distribution. This general approach has been realized and validated previously at NIST [3], and here is applied to the LPBF process, which is quite different from the one normally encountered in laboratory reflectometers. The scope of this paper is limited to the reflectometer design, performance of emissivity measurements, and evaluation of uncertainties.

The relatively small dimensions of the HAZ (with typical size of molten metal area less than 0.3 mm × 1.2 mm) and the dynamics of the process necessitate retrieval of spatially distributed data at a high spatial resolution. This comes at a cost of using a much more complicated sensor with relatively large imperfections and uncertainties as compared with a single element optical detector normally used in optical metrology [4]. In terms of requirement for reflectometry, this means using hemispherical illumination and directional (conical but within a small collection angle) imaging.

The temperatures encountered in a typical LPBF process range from room temperature to 3000 °C and above, with a special interest at the temperatures of the solidification and crystallographic phase changes (500 °C and above). Since the probing light of the reflectometer must compete with the self-emitted light from the hot scene, and in combination with

[1] david.deisenroth@nist.gov; phone 1 301 975-2594

the hemispherical-directional geometry (as mentioned above), this calls for an unusually high-power light sources in the reflectometer.

A further complication arises from the dynamic character of the process, in which the laser spot is scanned across the build area. Every frame of the imager is registered at a different location, which further complicates reflectance measurements due to sample spatial nonuniformity and possible defocusing of the laser. Since use of a stationary field of view will result in motion blur, it is customary to use imaging systems which share the scanning system with the process laser. This allows for avoidance of some problems with relative motion of the process and the field of view, but brings a new set of problems due to changes in focusing and optical path length for the wavelengths of the laser and reflectometry wavelength, as well as a lower collection efficiency due to the optics which are optimized for the laser wavelength to avoid damage by the high power laser. This results in additional uncertainties due to position-dependent defocusing of the laser and image.

Finally, there are some additional aspects of the process due to the presence of the process by-products (such as hot and condensed metal vapor), which require a directional flow of a shield gas which can significantly affect the process [5]. This introduces new sources of uncertainty, as well as further complicating the reflectometer design. Some of these effects have yet to be evaluated in detail, which is planned for a later date.

As stated previously, the scope of this paper is limited to the reflectometer design, the performance of emissivity measurements, and uncertainty evaluation. Section 2 describes the measurement approach, including the measurement equation, reflectometer design, and signal corrections for directional imaging. Section 3 details the uncertainty evaluation of test conditions, reflectometer illumination, and directional imaging. Finally, Section 4 describes measurement of a two-dimensional map of emissivity and emissivity uncertainty of the HAZ around a meltpool of high-purity nickel, followed with conclusions in Section 5.

2. EXPERIMENTAL SETUP AND MEASUREMENT APPROACH

The experiments were performed in the NIST Additive Manufacturing Metrology Testbed (AMMT) [6,7]. The AMMT is a custom LPBF research platform that is designed to be highly configurable for characterization of all aspects of the LPBF process. The AMMT includes a removable carriage that contains the build-well and a large metrology-well, both of which may be moved laterally within the large build chamber. The laser is an Yb-doped continuous wave (CW) fiber laser with an emission wavelength of 1070 nm. The delivered laser power can be adjusted from 20 W to about 385 W, with a 4σ diameter (D4σ, representing diameter within which about 95% of the Gaussian laser power profile is contained) spot size that is adjustable from 45 µm to more than 200 µm. The laser spot can be scanned with full control of the laser scan path/strategy at 100 kHz and laser power control at 50 kHz, with scan velocity of more than 4000 mm/s.

The core elements of the AMMT meltpool thermographic systems include (1) a high power fiber laser system emitting at 1070 nm; (2) an optical scanner (galvanometer), used to direct process laser spot; (3) beam splitter and optical components enabling co-axial meltpool imaging configuration; and (4) the sample under study, which can be accurately positioned and aligned with the object plane of the co-axial laser/imager optical path and is surrounded by an environmental enclosure with a shield gas flow. Additional thermographic equipment, which is referred to as the TEMPS system (Temperature and Emissivity of Melts, Powders, and Solids), includes an external (coaxial) imaging system, which is optically combined with the process laser and is used to measure the radiance distribution across the HAZ of the process.

An "indirect" method of emissivity measurement is employed in this work, in which the laser melting process is uniformly illuminated with uniform radiance across the hemisphere by a hemispherical reflectometer. The reflectometer uses a hemispherical-directional geometry, in which a ring of light emitting diodes (LEDs) around the equator of the hemisphere is optically integrated within the reflectometer to provide the uniform illumination. The laser melting scene is then imaged directionally through imaging optics that are coaxial with the heating laser, allowing for stationary viewing of the meltpool relative to the laser heating location. The measurement is performed once with the LED illumination on, and once with the LED illumination off. This approach facilitates spatially resolved radiance and reflectance/emissivity measurement of the meltpool. The measurement equation for emissivity will be discussed in the Section 2.1.

2.1 Measurement equation

The emissivity measurement equation for each single pixel of the focal plane array (FPA) is as follows:

$$\varepsilon_\lambda(\lambda_o, T_s) = 1 - C_\rho \rho_{ref} \frac{S_{samp}^{LED\ On}(\lambda_o,T_S) - S_{samp}^{LED\ Off}(\lambda_o,T_S)}{S_{ref}^{LED\ on}(\lambda_o) - S_{ref}^{LED\ off}(\lambda_o)} \tag{1}$$

where ε_λ is the spectral normal (or 8°) spectral emissivity of the sample, λ_o is the central wavelength of the radiometer (and the light source), T_S is the sample temperature, and ρ_{ref} is the reflectance of the calibrated reference standard. The linearized signal measured by a single pixel of the imager is denoted by S. The signal linearization approach and its uncertainties will be discussed in Section 2.3.1. The superscripts "LED on" and "LED off" refer to signals obtained with and without LED illumination. The subscripts "samp" and "ref" refer to the objects of measure: the sample and the calibrated reflectance standard, respectively. The term C_ρ has a nominal value of one and is used as a correction factor for systematic biases. It has an associated uncertainty, which is propagated into the uncertainty of ε_λ. The correction factor C_ρ is comprised of multiple correction factors, which are associated with each source of bias, non-ideality, and uncertainty associated with the reflectometer:

$$C_\rho = C_{TU} C_{PL} C_{LED} C_{ARM} C_{AS} C_{BRDFS} C_S \tag{2}$$

where C_{TU},C_{PL}, C_{LED}, C_{ARM}, C_{AS}, C_{BRDFS},and C_S are the factors associated with throughput uniformity, port losses and high angle losses, LED reproducibility, alignment of the reference mirror, alignment of the sample, the sample bi-directional reflectance distribution function (BRDF, discussed in Section 3.1.4), and out of field scatter, respectively. Section 2.2 will describe the important design considerations of the reflectometer used for these measurements.

2.2 Baffle-less center-mount reflectometer design features

The design of the reflectometer is constrained by the size of the build chamber, the necessary gas flow provisions for laser-metal interaction, fabrication limitations, and the likelihood of damage to the reflective coating by laser reflection from the melting process. In the current case, a hemispherical reflectometer design is used instead of a complete sphere in order to address the unique considerations of the LPBF environment, while maintaining illumination performance. Use of integrating hemispheres have been applied for compact size and other optical considerations, but have not yet been applied to emissivity measurement of the LPBF to the best of our knowledge [8].

With respect to port size ratio, use of a hemisphere instead of a complete sphere allowed for a smaller laser-entrance port size and sample port size, relative to the total integration area, while fitting within the height of the build chamber of the AMMT. An equivalent height complete integrating sphere would have had about double the port area to integration area ratio. With respect to coating damage, the hemispherical design allowed the integrating surface to have greater average distance from the process, ranging from the same distance at the entrance port to double the distance at about 22° from horizontal. At normal incidence, irradiance (radiant flux received by a surface in units of W/m^2) is proportional to the square of distance, and so the hemispherical design reduces the diffuse coating exposure to intense laser reflections on average by about a factor of two. Furthermore, the hemispherical geometry allowed for double the perimeter for LED illumination, also facilitating double the intensity of illumination which must be on the same order of magnitude of the process self-emission.

A cross-sectional view of a computer aided design model of the integrating hemisphere is shown in Figure 1. As shown, optical integration is facilitated by a diffuse, barium sulfate coating and with a specular, polished aluminum base electroplated with gold, which has excellent reflectivity at 850 nm. The reflected light from the hemispherical illumination is imaged through an elongated port on the top of the hemisphere, about 8° from the vertical. The 8° offset of the port prevents retroreflection from a specular (or nearly specular) sample into the inline optics, reducing the possibility of incomplete and/or nonuniform illumination of the sample due to the detection port. Furthermore, in the case of the current application, reduced likelihood of retroreflection from the sample into the inline optics also reduces the possibility of damage to the filters or the imager from retroreflected high-power laser light. The elongated design of the laser port and sample port enables scans to be performed within an area of about 3 mm × 20 mm with coaxial imaging of the laser-metal interaction scene.

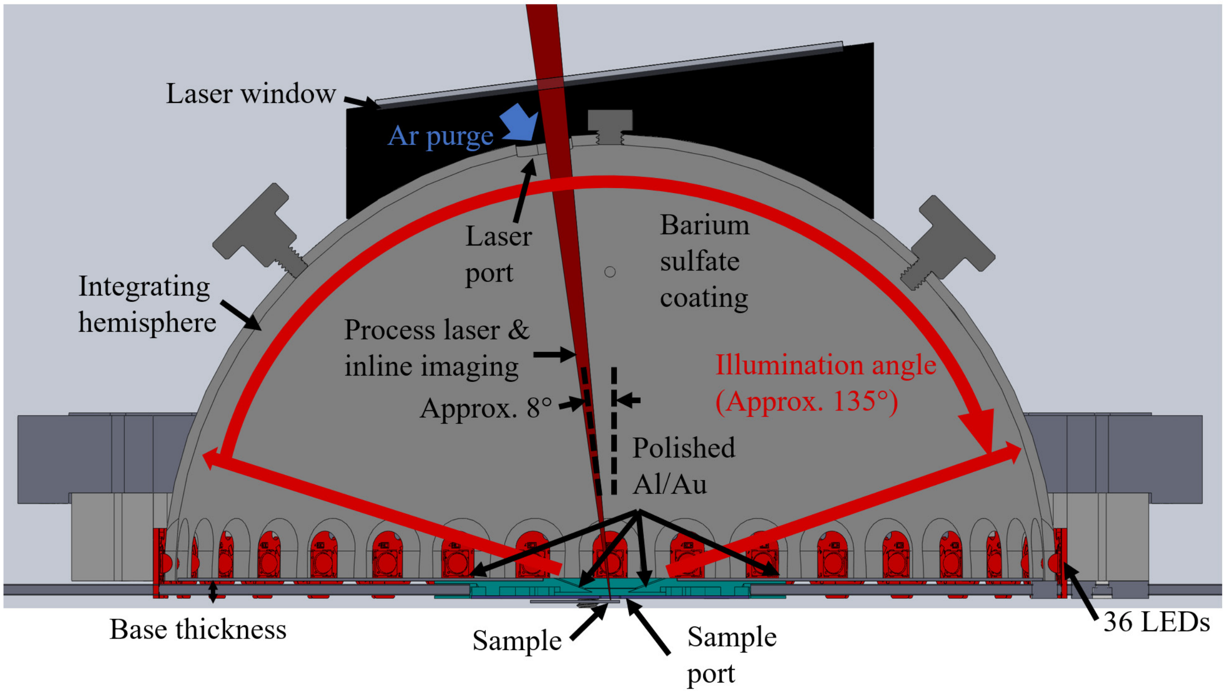

Figure 1. Cross-sectional view of a computer aided design model of the integrating hemisphere.

Another design constraint unique to the LPBF environment is that inert gas atmosphere is required for laser melting in order to reduce detrimental oxidation [9(p3)]. Previous studies have shown that directional and inert shield gas flow is essential to facilitate continuous, consistent beam delivery by removing process biproducts that can distort, scatter, and obstruct beam delivery [10,11]. As shown in Figure 1, Ar gas is pumped into the reflectometer through the laser port. The gas flow rate is typically about 30 L/min, which results in a downward flow onto the sample of about 0.5 m/s, which provides some byproduct removal. Future tests will incorporate an improved directional gas flow provision. In the current investigation, laser scanning occurred in the direction perpendicular to the image plane of Figure 1.

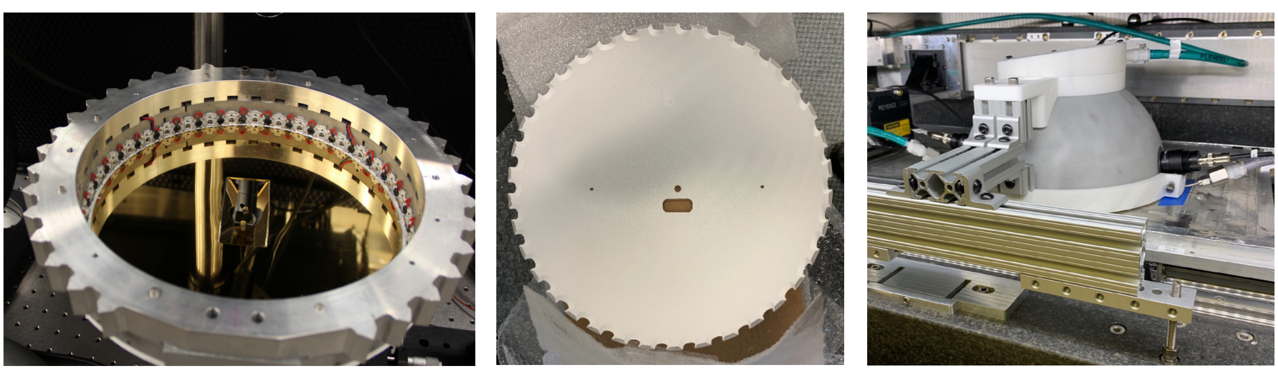

(a) **(b)** **(c)**

Figure 2. Images of the fabricated integrating hemisphere: (a) the specular base assembly, (b) the barium sulfate coated hemisphere interior, and (c) the assembled apparatus mounted in the build chamber.

The surfaces near the sample port are angled at about 22°, as shown in Figure 1. This creates a base thickness of about 6.7 mm. The thickness of the base of the dome acts as a baffle and results in an illumination angle of about 135°, as shown in Figure 1. The LEDs are located as close as possible to the equator of the hemisphere. At this location, the base thickness has a beneficial baffle-effect, and prevents deleterious direct illumination of the sample by the LEDs, which would lead to nonuniform illumination. The base thickness, though, causes a loss of light in the remaining 45° of the hemisphere, which does not contribute to illumination. In practice, surface features reflecting light into the directional imaging path at an angle less than 22° from the horizontal are unlikely, but possible, and the associated contribution to surface reflectance/emissivity measurement uncertainty must be evaluated. The fabricated base, hemisphere interior, and assembled integrating hemisphere within the build chamber are shown in Figure 2. Each source of error and uncertainty associated with the reflectometer-based measurement of emissivity will be described in Section 2.3.

2.3 Directional imaging signal corrections

The corrections used to condition the signal used for the measurement of spatially resolved emissivity will be described at length in a forthcoming publication, hence these items will be only briefly summarized in this section. Two primary corrections are applied to the signal: 1) the erroneous signal components due to stray light and blooming are subtracted, and 2) the images are deconvolved with a blur kernel to compensate for image distortion due to the optical blur and finite pixel size of the FPA. The corrections are applied to each image of the 30 central images of the test sequence to avoid transients due to startup and laser shutoff.

In this work, motion blur is not considered because the image is static relative to the laser motion, making the meltpool quasi-static in this reference frame. Although the meltpool undulates slightly relative to the laser motion, blur due to meltpool length changes and location variability within the reference frame within the integration time is assumed to be negligible.

2.3.1 Linearization with radiant flux

The imager signal must be linearized with respect to the object radiant flux for accurate determination of the emissivity. The imager signal is linearized by exposure to the steady, known radiance of a high temperature blackbody (HTBB). The imager is outfitted with a long working distance microscope lens body and objective lens, a band filter, and a laser cutoff filter. The measurement equation for linearization is then as follows:

$$S(T)_{cal} = C_{cal,BB} \int_{\lambda 1}^{\lambda 2} \tau_{\lambda}^{obj}(\lambda) \tau_{\lambda}^{filt}(\lambda) r_{\lambda}^{FPA}(\lambda) \frac{c_{1L}}{\lambda^5 \left[exp(\, c_2/(\lambda T_{rad,BB})) - 1 \right]} d\lambda \tag{3}$$

where the pixel signal $S(T)_{cal}$ is the FPA signal, $\tau_{\lambda}^{obj}(\lambda)$ is the spectral transmittance of the objective lens, $\tau_{\lambda}^{filt}(\lambda)$ is the filter spectral transmittance, and $r_{\lambda}^{FPA}(\lambda)$ is the imager spectral responsivity, c_{1L} and c_2 are the first and second radiation constants, λ is wavelength, and $T_{rad,BB}$ is the radiance temperature of the HTBB. The signal is linearized with the single-point averages of image sequences at varying HTBB temperatures. This can be done because of the relatively low noise and FPA nonuniformity, both of which are incorporated into the measurement uncertainty. Once $C_{cal,BB}$ is determined at a single point, the signal at each HTBB temperature is linearized using Equation (3) to generate a linearization function for the signal.

2.3.2 Stray light and blooming correction

Stray light is light that passes through the optical system in a manner that is not intended in the optical system. Imager blooming occurs when a pixel potential well is overfilled and the excess charge bleeds over into adjacent pixels. Both stray light and blooming tend to increase the FPA signal near high intensity regions, typically exhibiting exponential decay in erroneous signal with distance from the high intensity regions. Although the TEMPS optical system is designed using best practices to reduce stray light [12] and the imager with complementary metal–oxide–semiconductor (CMOS) is relatively impervious to blooming, these effects must be measured and compensated for high accuracy measurements. Our measurements indicate that the meltpool hotspot generates about 100 times more radiant flux than the intensity levels of interest near the melting temperature, which produces a significant potential for erroneous signal due to stray light and blooming.

Stray light and blooming are be measured simultaneously because both have similar causes and effects on the measurements. In order to quantify the combined effect of stray light and blooming, an illumination source other than the meltpool is required to eliminate the optical effects of the laser-melting process variability and byproducts. The source chosen for the application is a 6 µm diameter fiber coupled laser with divergence angle exceeding the acceptance angle of the TEMPS optics. The fiber-coupled laser is located under an aperture located at the build plane height so that the aperture is slightly overfilled. Illumination is projected onto the imager through the TEMPS optics system to replicate the meltpool hot spot. The aperture size and intensity are selected to closely mimic the area and intensity of the meltpool hotspot.

A curve fit is performed on the erroneous signal generated outside of the 100 µm aperture. The center of the hotspot is then located and the distance of the center of each pixel from the hotspot center is calculated. The erroneous signal at each pixel due to stray light and blooming is calculated from the curve fit based on the pixel distance from the hotspot. Finally, the erroneous signal is subtracted from each meltpool image of interest. The pixels in the saturated region are left at the original saturated digital level (DL). After subtraction of the signal due to stray light and blooming, a mild smoothing operation is then applied to images.

2.3.3 Image smoothing

A mild smoothing filter is applied to each test image after the stray light and blooming subtraction. Smoothing the images reduces the effects of noise on the deconvolution. The smoothing filter is based on nearest-neighbor averaging with one adjacent pixel on either side, top and bottom. We confirmed that the smoothing operation does not introduce a systematic signal bias by subtracting the original image from the smoothed image and averaging across the frame. The resulting average signal difference has been found to result in a negligible average bias of less than 1% of a digital level at each pixel.

2.3.4 Image deconvolution

Deconvolution is an image processing operation intended to reconstruct an image to its original form prior to blur induced by inevitably non-ideal optics and finite pixel size of FPAs. The multistep deconvolution approach taken here is based on that of Lane and Whitenton [13] and ISO 12233:2017 [14]. First, a knife edge measurement is taken to establish an edge spread function (ESF). The ESF is then transformed into a point spread function (PSF), which can be thought of as a "deblurring kernel." Finally, the images are deconvolved. The details of each element of the operation are discussed.

2.3.4.1 Knife-edge measurement

Use of an ESF measurement is a practical approach to the determination of the PSF, because use of a true point source is experimentally difficult, if not impossible [14]. Use of an ESF to determine the PSF reasonably assumes that the response of the optical system is rotationally symmetric.

To establish the ESF, a thin, opaque, and straight edge is placed to partially cover the aperture of the thermal integrating sphere source with 850 nm center wavelength (TISS850) set at a radiance temperature of 1600 °C at the build plane. The TISS850 is transfer source developed in the AMMT that is composed of LEDs that are thermally stabilized (by ethanol heat pipes cooled by a thermoelectric cooler and fan) to illuminate a polytetrafluoroethylene (PTFE) integrating sphere that generates uniform illumination at the waveband of interest—brightness that is calibrated against the HTBB thermal source. The edge is placed a few degrees from vertical so that it is not perfectly aligned with the pixel array [13,14]. Sampling lines are then taken perpendicular to a curve fit of the maximum image gradient to mark the edge between the high and low DLs. The image data are taken with a resolution of 6.0 µm per pixel through the TEMPS optics and the imager is set to a shutter speed of 98.3 µs, which is followed by determination of the ESF.

2.3.4.2 Edge spread function determination

The four sampling lines across the knife-edge image are found to be negligibly different, and so one of them is taken as representative of the image profile. The representative profile is then normalized to have a peak intensity of unity and is supersampled with 4 samples per pixel along the length of the array, per ISO 12233:2017 [14]. The data is then centered on zero based on the maximum gradient of the profile. In sampling with one, two, and three component error function fits, it is found that the most appropriate fit is with the two-component error function shown in Equation (4), with $R^2 = 0.998$.

$$\mathrm{ESF} = a_1 \operatorname{erf}\frac{x}{b_1} + a_2 \operatorname{erf}\frac{x}{b_2} + 0.5 \tag{4}$$

where x is distance in pixels, $b_1 = 3.184$ [pixels], $a_2 = 69.04$, and $b_2 = 3.184$ [pixels].

2.3.4.3 Point spread function determination

The PSF is determined from the ESF via differentiation followed by an Abel Transform as per Lane and Whitenton [13]. The corresponding PSF is shown in Equation (5).

$$\mathrm{PSF} = \frac{2}{\pi}\frac{a_1}{b_1^2}\exp\left(-\frac{r^2}{b_1^2}\right) + \frac{2}{\pi}\frac{a_2}{b_2^2}\exp\left(-\frac{r^2}{b_2^2}\right) \tag{5}$$

where r is the radial distance in pixels, and a_1, b_1, a_2, and b_2 are the values determined from Equation (4). The value of the PSF array is calculated at each super-sampled pixel location using Equation (4), and then averaged across the 4 × 4 super-sampled pixel to determine the PSF value at each pixel. The resulting PSF array is 25 pixels × 25 pixels in order to cover four orders of magnitude of intensity from the PSF center to the perimeter. The volume under the PSF array is finally normalized to unity.

2.3.4.4 Deconvolution

The final step is the deconvolution operation. Each image of the central 30 images of the test sequence is individually deconvolved to allow for later uncertainty analysis of the deconvolved image transient variability. Each image is first corrected for stray light and blooming, then smoothed as discussed in the preceding sections. The PSF array is then used to deconvolve each image with the MATLAB[2] 'deconvlucy' function, which is based on the iterative Richardson-Lucy method [15,16].

It is observed that the image is "sharpened" after deconvolution. The sharpening causes an apparent narrowing of the meltpool and steepening of the signal gradients on the left and right side, as well as at the nose. Toward the end of the tail, the local signal gradient becomes shallower and longer along the length of the meltpool, but steeper in the transverse direction across the tail.

2.3.5 Summary of the effects of signal corrections

The effect of each image correction operation is shown by a central cross-sectional profile along the length of the meltpool in Figure 3. Beginning with a linearized signal, the stray light and blooming subtraction operation reduces the signal at the nose of the meltpool because of its proximity to the hotspot, but has a very small effect on the signal at the tail because of its larger distance from the hotpot. The smoothing operation has very little effect on the signal levels but reduces the apparent pixel to pixel noise.

Deconvolution tends to have the most notable effect on the signal levels, both at the nose and tail of the meltpool. Deconvolution sharpens the profile, reducing the signal at areas of high curvature (large values of the second derivative), and steepening the profile at areas of high (two-dimensional) gradients. This can be observed at the nose and tail of the meltpool at pixel 10 and 48, respectively. The most significant variation in the central cross-sectional profile due to deconvolution occurs in the tail, where a "solidification plateau" appears. At this solidification plateau from pixel 59 to 63, the signal is flat, indicating an apparently isothermal solidification region as the laser heat source moves. This isothermal region is expected in the solidification process of high purity metals (99.998% Ni used here), because the fixed-point freezing temperature at which the phase change occurs is maintained as the material dissipates the latent heat of fusion at the solidification temperature. The solidification region is made significantly more apparent in the signal by deconvolution. The signal uncertainty incurred by each signal correction operation will be discussed in Section 3.

[2] Certain commercial entities, equipment, or materials may be identified in this document to describe an experimental procedure or concept adequately. Such identification is not intended to imply recommendation or endorsement by the National Institute of Standards and Technology, nor is it intended to imply that the entities, materials, or equipment are necessarily the best available for the purpose.

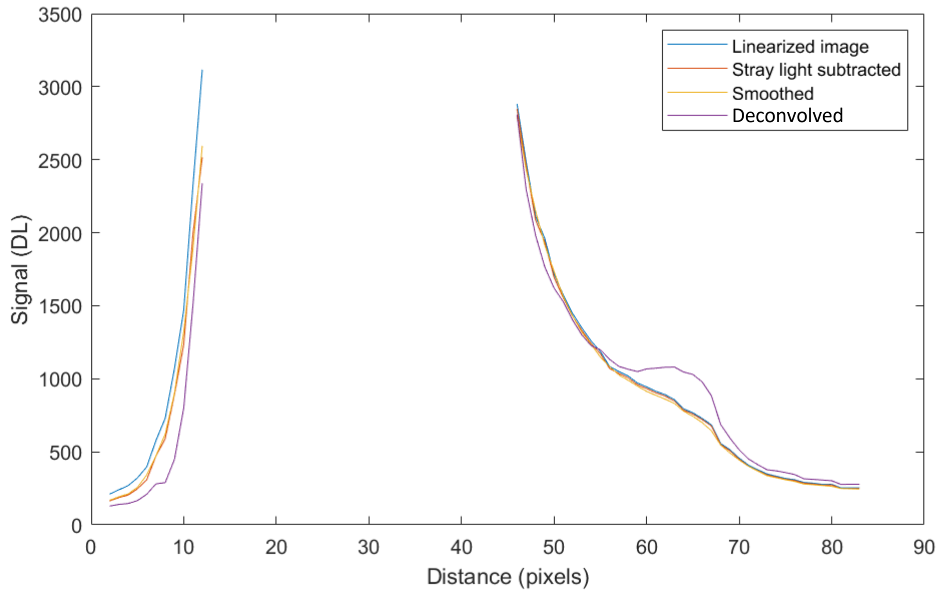

Figure 3. Central cross-sectional profile along the length of the meltpool showing the effect of each image correction. Meltpool nose is on the left and tail is on the right.

3. UNCERTAINTY

Three categories of sources of emissivity uncertainty have been identified. The first includes the nonideality, misalignment, and uncertainty in reflective character of the reference mirror and the sample. The second includes nonuniformity and incomplete hemispherical illumination, which pertains to the nonideality of the reflectometer. The third and final category of uncertainty is the nonideality of the directional imaging system, including the inline optics, imager, and image corrections.

3.1 Sample and reference uncertainties

3.1.1 Reference mirror alignment

As was discussed previously, both specular and diffuse reference samples are used in emissivity measurement and evaluation of uncertainties. The angular alignment and distance from the reflective surface to the reflectometer sample port (gap) slightly alter illumination of the reflector, as well as the reflectometer throughput (the throughput is the ratio of the flux reaching the detector to the input flux from the source). In the case of the specular mirror, misalignment or increased gap changes the location on the integrating surface from which the sample is illuminated, while also reducing throughput due to light loss from the gap. In the case of the diffuse reflectance standard, a misalignment or increased gap size changes the magnitude and location of the solid angle from which the reflector is illuminated. An experiment was performed to measure the relative change in signal when the specular reflectance standard was moved relative to the floor of the reflectometer (located at 219.3 mm from the laser window), as shown in Figure 4.

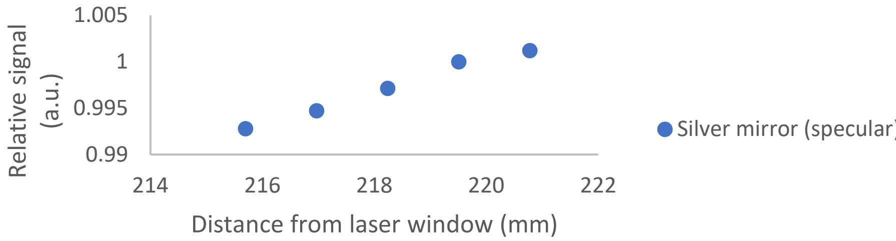

Figure 4. The relative signal measured as a function of the specular reflectance standard location relative to the laser window, with the floor of the reflectometer located at 219.3 mm

The reference mirrors are aligned with a laser displacement meter, which has an uncertainty of 1 µm (k = 1), and the reflectometer is mounted on kinematic mounts for accurate repositioning. The rotational misalignment is assumed to be negligible. It is conservatively estimated that the reflectance standard is located within ±1 mm, for which the relative range of the signal is 0.6 % (or equivalently ±0.3 % of the midpoint within the relative range). The signal has a uniform probability of being within that range, so dividing by $\sqrt{12}$, the signal uncertainty is 0.2 % [17]. Therefore, the nominal value of C_{ARM} is 1.0 with a relative standard uncertainty of 0.002.

3.1.2 Reference mirror reflectance

The reflectance standards used in these experiments are calibrated by NIST. The uncertainty in reflectance is 0.5 % [18]. Therefore, the nominal value of ρ_{ref} is 0.97 with a relative standard uncertainty of 0.005.

3.1.3 Sample gap and alignment

The effects of sample gap changes and misalignment are similar to those for the reference mirror—changes in this affects where the location from which illumination occurs on the integrating surface is, and thus the resulting throughput of the reflection. Currently, the best approximation of the effect of sample alignment is from measurements taken with a diffuse reflective standard sample (pressed polytetrafluoroethylene PTFE) and a sample with a diffuse-directional reflective character between perfectly specular and diffuse (brushed stainless steel). The results of gap change between the reflectance standards and the laser window (with the reflectometer floor located at 219.3 mm from the laser window), is shown in Figure 5.

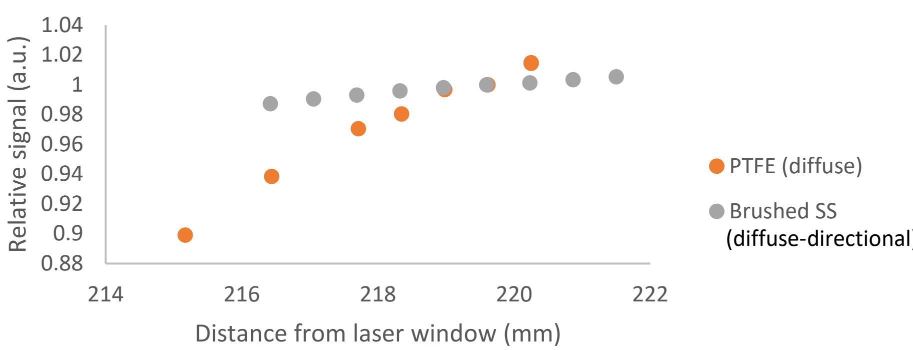

Figure 5. Relative signal measured as a function of the location of two reflectance standards relative to the laser window, with the floor of the reflectometer located at 219.3 mm

The samples of high-purity Ni for generating laser-induced meltpools are aligned with the laser focus as described above, but with a tolerance of ±20 µm (vertical misalignment is generated by surface non-flatness, general roughness, and tilt). Rotational misalignment is again assumed to be negligible. Assuming location within ±1 mm as above, and that the diffuse reflectance standard is representative of the maximum change in reflectance of a real sample (e.g., stainless steel reflectance sample, or laser-induced melt pool), the relative range of signal is about 5.0 % (or equivalently, about ±2.5 %

from midpoint of the range). Assuming a uniform distribution within this range, the relative standard uncertainty of C_{AS} becomes 1.5 %. Therefore, $C_{AS} = 1.0 \pm 0.015$.

3.1.4 Sample bidirectional reflectance distribution function

The sample BRDF is a mathematical function that describes how the hemispherical illumination of the sample is reflected and imaged by the directional imaging system. Currently, very little is known or has been measured regarding the reflective character of the laser-metal interaction scene and is an important area for future investigation. In the absence of additional information, the sample BRDF is assumed to have a similar effect to the throughput uniformity (discussed in Section 3.2.1) with no bias. Therefore, $C_{BRDFS} = 1.0 \pm 0.01$. It should be noted that under certain specific (relatively unlikely) circumstances, the sample BRDF could be a dominant uncertainty component.

3.1.5 Summary of sample and reference uncertainties

The uncertainties due to the sample and reference conditions are summarized in Table 1, where C_{ARM}, C_{AS}, C_{BRDFS}, and C_S are defined in Section 2.1. The reflectance of the reference mirror is ρ_{ref}.

Table 1: Summary of uncertainties due to sample and reference conditions

Variable	***Value***	***Units***	***Relative uncertainty (k = 1), (%)***	***Type***
C_{ARM}	1	-	0.2	A
C_{AS}	1	-	1.5	B
C_{BRDFS}	1	-	1.0	B
C_S	0.9975	-	0.5	B
ρ_{ref}	0.97	-	0.5	A

3.2 Nonuniform and incomplete hemispherical illumination

3.2.1 Throughput uniformity

Reflectometer throughput is the ratio of the flux reaching the detector to the input flux from the source. Relative throughput is measured across the integrating surface and reported in arbitrary units. Relative throughput mapping of the inside of the hemisphere quantifies the uniformity of hemispherical illumination of the reflectometer as a whole and allows estimation of the measurement uncertainty. Throughput mapping is performed by placing a photodetector at the entrance port and a gimbal-mounted mirror is located at the sample port. The mirror is aimed at a representative number of locations across the inside of the hemisphere.

As shown in Figure 6, the throughput uniformity of the surface is within ±1.0 % across from about 5° from the vertical to about 80°. Decreased radiance throughput occurs at the imaging port (5° to 15°), at the monitoring diode ports (45°), and increased high angle losses occur opposite to the port at 70° to 90°. The main features and nonidealities of the reflectometer are detected at these locations, and the uniformity around these features is taken as representative of the remainder of the reflective surface. From these results, the throughput uniformity we can assume a negligible bias in the emissivity calculation and the uncertainty is taken to be 1.0 %. Therefore, the nominal value of C_{TU} is 1.0 with a relative standard uncertainty of 0.01.

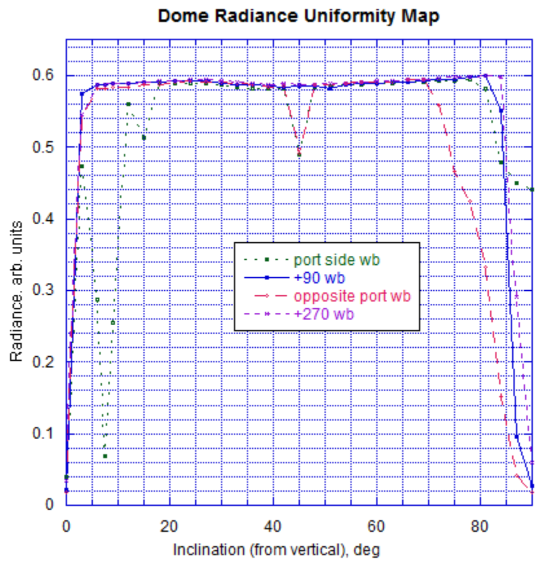

Figure 6. Relative throughput of the hemispherical integrating surface for four orthogonal cross sections. The tests are performed with the specular gold base (wb).

3.2.2 Port losses and high-angle losses

The light loss due to the laser port and base thickness on the first reflection from the sample are measured by comparing the measured signal with a specular silver standard and a diffuse gold standard. On the first reflection, a specular sample does not result in any port loss or high angle loss. In contrast, a perfectly diffuse sample results in both high angle and port losses. After accounting for the reflectivity of the samples, it is found that 2.5 % in intensity is lost for the diffuse sample as compared to the specular sample. The laser-metal interaction scene is likely better represented by a value in between the specular and diffuse cases, so the bias is assumed to be of the average of the losses for the two samples plus or minus half of the difference. Then the nominal value of C_{PL} is 1.013, with a standard uncertainty of 0.013.

The reflective character of the laser-metal interaction scene is a significant unknown and could potentially result in greater port losses and high angle losses than those considered here. Therefore, two approaches have been identified to better quantify the emissivity uncertainty component due to port losses and one approach has been identified for estimating high angle losses.

The first approach to estimating port losses is to reduce the size of the port to as small as possible, which would require a shortened laser scan distance. The relative change in signal compared with the normal port size can then be used to calculate a more representative port loss. The second approach is to add a supplementary light source via a beam splitter directed along the imaging path to add additional light from the port area, which will then be optically integrated in the reflectometer. The additional signal may then be used to better quantify port loss bias and uncertainty.

To estimate high angle losses, a small sample is moved upward through the base of the reflectometer with an adjustable cylindrical baffle surrounding it. The motion of the sample relative to the baffle and reflectometer base and the resulting change in signal intensity will be used to quantify the effect of high angle losses. The high angle losses are expected to be negligible under most circumstances, but the high-angle loss test raises concerns about scattering and absorption in the process plume and how to deconvolve those effects from high-angle loss effects, which must be addressed. Nevertheless, the combined port loss and high-angle loss estimate reported here is should be acceptable under most conditions.

3.2.3 Coating reflectance and diffuseness

Both the reflectance and the specularity of the integrating sphere coating can have an effect on the size of the potential measurement error and resulting uncertainty, with more reflective and more diffuse coatings resulting in more accurate measurements [19,20]. The barium sulfate coating used in this application has a highly diffuse reflectance with a directional-hemispherical reflectance of 0.981 at 850 nm [21]. Therefore, the coating reflectance and diffuseness is expected to have a negligible effect on the accuracy of measurements in the given application and are therefore omitted from Equation (1) and the uncertainty budget.

3.2.4 LED reproducibility

The intensity and spectrum of the illumination LEDs change as the junction temperatures increase within the semiconductor devices. According to the manufacturer's datasheet, the radiant flux output decreases by as much as 35 % when the LED case temperature changes from room temperature to 100 °C, and the peak wavelength shifts by 13 nm [22]. The absolute shift in output and wavelength are not of high importance alone, but the reproducibility of the output from the sample and the reflectance standard introduces an additional uncertainty component in the emissivity measurement. We have tested reproducibility of the LED illumination previously and estimate that it induces an uncertainty of 1.5 % in the LED correction factor C_{LED}. Stochastic non-reproducibility does not induce a bias. Hence, the nominal value of C_{LED} is 1.0 with a relative standard uncertainty of 0.015.

The uncertainty component associated with LED reproducibility can be measured with repeat tests using the reflectance standard while recording the signal received by the imager. This uncertainty component can also be reduced with combined triggering of the LEDs with triggering of the imager and laser scanning system.

3.2.5 Summary of uncertainties due to nonuniform and incomplete illumination

The uncertainties associated with nonuniform and incomplete illumination are summarized in Table 2, where C_{TU},C_{PL}, and C_{LED} are defined in Section 2.1.

Table 2: Summary of uncertainties due to nonuniform and incomplete illumination

Variable	*Value*	*Units*	*Relative uncertainty (k = 1), (%)*	*Type*
C_{TU}	1	-	1.0	A
C_{PL}	1.013	-	1.3	B
C_{LED}	1	-	1.5	B

3.3 Directional imaging

Nine sources of uncertainty in the FPA signal are considered in addition to the aforementioned measurement uncertainty components in the measurement equation (Equation (1)), as follows:

1. Out of field scatter from sample port surfaces
2. Polarization effects
3. Linearization uncertainty
4. Uncertainty due to stray light and blooming correction
5. Uncertainty due to image smoothing
6. Uncertainty due to point spread function determination
7. Uncertainty due to deconvolution operation
8. Uncertainty due to deconvolved signal variability caused by process variability and imager noise
9. FPA nonuniformity

This section describes the uncertainty of the corrections, as well as the resulting uncertainty of the measured emissivity.

3.3.1 Out of field scatter from sample port surfaces

The edges of the reflectometer sample port are a non-ideality that may cause out of field scatter that may be detected as erroneous signal by the directional imaging system. This effect is expected to be small, and in the absence of experimental data, it is assumed to induce an increase of signal bias of 0.25 % with a (Type B) relative standard uncertainty of 0.5 %. Therefore, $C_S = 0.9975$ with a relative standard uncertainty of 0.005. The port surfaces may be coated with absorptive (black) paint in the future to reduce the associated bias and uncertainty of out of field scatter.

3.3.2 Polarization effects

Polarization may significantly alter the throughput uniformity of integrating spheres and should be considered as a potential uncertainty component [23]. The integrating hemisphere uses 36 symmetrically distributed LED sources for illumination, which means that the illumination is very unlikely to have a preferred polarization illumination of the sample or reference mirror. The samples used for meltpool generation are randomly sanded, making the un-melted material unlikely to have preferred polarization reflectivity. The Ag reference mirror has very low polarization at 850 nm and at the 8° from normal reflection angle, making reference mirror polarization bias unlikely. Finally, nearly all practically useful data are obtained on molten or re-solidified sample surfaces, which have potential for polarizing effects, but this has not yet been measured. In the future, a series of tests will be performed with varying scan direction and rotation of the randomly sanded sample to quantify polarization effects. Currently, measurement bias and uncertainty of emissivity due to polarization is assumed to be negligible.

3.3.3 Imager signal linearization uncertainty

The primary instrument used for the emissivity measurement uses a CMOS FPA. The imager has a 1024 pixel × 1024 pixel, 12-bit dynamic range FPA. In this work, all data are obtained with a shutter speed of 98.3 µs. The transient pixel noise and nonuniformity across the FPA are sources of signal variance and therefore contribute to the measurement uncertainty. Furthermore, the nonlinearity of the signal with the incident flux requires correction by calibration to a known-flux source, which introduces an additional uncertainty component for the signal. Each of these are discussed in this section.

In order to evaluate the uncertainty due to transient pixel noise, the HTBB is used as a stable source. The imager is outfitted with an long working distance microscope lens body and an objective lens focused at the HTBB aperture to generate uniform and steady irradiance of the FPA. The majority of the signal variation is therefore due to electronic noise. The nonuniformity of the blackbody irradiation is considered to be negligible in this evaluation. The GainCal function in the imager software is used for flat-fielding (or, nonuniformity correction) to reduce the natural optical vignetting and improve the pixel uniformity across the FPA.

3.3.3.1 Pixel noise and FPA nonuniformity

Samples of 100 images are taken with varying HTBB set-point temperatures. Then the standard error (SE) of the mean DL of each pixel is determined from the 100-image sample. Use of the dynamic range is limited to between 300 DL and 3800 DL, which results in a transient pixel noise relative standard uncertainty component of the signal of 0.3 %.

Images from the linearization against the HTBB are used to measure the FPA nonuniformity. The pixel average is taken from the 100-image sample, resulting in a calibration image with the average DL of each pixel. The standard deviation across the pixel array is then determined to evaluate the nonuniformity across the FPA. The resulting frame standard deviation of the pixel average is expressed as a percentage of the DL. Use of the dynamic range is limited to between 300 DL and 3800 DL, which results in an FPA nonuniformity relative standard uncertainty component of the signal of 1.0 %. The combined transient pixel noise and FPA nonuniformity relative standard uncertainty is then 1.05 %.

3.3.3.2 Spectral variable uncertainties

In order to solve Equation (3), the lens spectral transmission $\tau_\lambda^{obj}(\lambda)$, filter spectral transmission ($\tau_\lambda^{filt}(\lambda)$), FPA spectral responsivity (r_λ^{FPA}), and HTBB temperature (T_{BB}) must be measured. Inspection of Equation (3) shows that the absolute biases of the spectral quantities will simply change the value of $C_{cal,BB}$, which does not affect its uncertainty. Therefore, deviation in the magnitude of the spectral values across the waveband of interest are used to evaluate the uncertainty of $C_{cal,BB}$.

The measured spectral responsivity of the FPA is measured with an instrument with a conservatively estimated relative standard uncertainty of 2.0 %. The worst case of the value varying from its minimum value of $0.98r_\lambda^{FPA}(\lambda)$ to $1.02r_\lambda^{FPA}(\lambda)$ from 830 nm to 870 nm is then used to evaluate the change in $C_{cal,BB}$. Because of the wide and uneven spectral spacing of the data points, interpolation of the values is used. All values of the spectral quantities used in Equation (3) are evaluated at the same uniformly gridded values of λ, and their product is integrated using trapezoidal summation.

The measured spectral transmission of the combined 850 nm ± 20 nm bandpass filter and the 1000 nm laser cutoff filter is also measured, and the spectrometer used to measure the transmission is known from previous evaluations to have a relative standard uncertainty of 0.5 %. The worst cases of the value varying from its minimum value of $0.995\tau_\lambda^{filt}(\lambda)$ to $1.005\tau_\lambda^{filt}(\lambda)$ from 830 nm to 870 nm is used to evaluate the change in $C_{cal,BB}$. Finally, the transmission of the camera lens assembly is conservatively assumed to have a relative standard uncertainty of 2.0 % across the waveband of interest.

3.3.3.3 Wavelength and radiance uncertainties

The spectrometer used to measure the transmission of the filters has a spectral resolution of 0.5 nm, which we use as the uncertainty in λ. The uncertainty of the blackbody radiance ($L_\lambda^{BB}(\lambda)$), defined in Equation (6), has been determined to be 0.6 % and which will be described in detail in a forthcoming publication.

$$L_\lambda^{BB}(\lambda) = \frac{c_{1L}}{\lambda^5\left[exp(\,c_2/(\lambda T_{rad,BB})) - 1\right]} \tag{6}$$

3.3.3.4 Combined uncertainty due to linearization

The combined uncertainty of the calibration constant is calculated by first evaluating Equation (3) with each variable in its worst case, or maximum uncertainty. This establishes the sensitivity of the calibration constant to each uncertainty component. Then, the sum-square of all the uncertainty components is taken to evaluate the combined uncertainty of the calibration constant. These results are shown in Table 3.

Table 3. Combined signal and linearity uncertainty components of the calibration constant $C_{cal,BB}$.

Variable	Uncertainty (k = 1)	Type	Change from nominal value	Change in $C_{cal,BB}$ (%)
$\tau_\lambda^{filt}(\lambda)$	0.5 %	B	Increasing with λ	-0.01
			Decreasing with λ	0.01
$\tau_\lambda^{CF1}(\lambda)$	2.0 %	B	Increasing with λ	-0.05
			Decreasing with λ	0.05
$r_\lambda^{FPA}(\lambda)$	2.0 %	B	Increasing with λ	-0.05
			Decreasing with λ	0.05
λ	0.5 nm	A	Absolute increase	-0.48
			Absolute decrease	0.48
$L_\lambda^{BB}(\lambda)$	0.6 %	A/B	Absolute increase	-0.6

			Absolute decrease	0.6
$S(T)_{cal}$	1.05 %	A	Absolute increase	1.00
			Absolute decrease	-1.00
			Combined uncertainty of $C_{cal,BB}$	**1.25**

3.3.4 Stray light and blooming

The range-normalized root mean square error (RMSE) of the curve fit applied to the erroneous signal due to stray light and blooming is 0.7 %. This is used as the uncertainty of the curve fit to the stray light and blooming signal matrix, combined with the uncertainty due to noise in the knife-edge measurements. As described in Section 3.3.3.4, the uncertainty of the signal linearization operation is 1.25 % and this is taken as an additional uncertainty. The combined uncertainty of the stray light and blooming correction is then 1.4 % of the DL of each pixel of the erroneous signal matrix, which is calculated for the uncertainty of each pixel of the stray light and blooming corrected image.

3.3.5 Image smoothing

As stated previously, it is confirmed that the smoothing operation does not introduce a systematic bias. This is demonstrated by subtracting the original image from the smoothed image and averaging across the frame, resulting in a negligible bias of less than 1% of a digital level per pixel. Therefore, the uncertainty due to image smoothing is taken to be negligible.

3.3.6 Point spread function uncertainty

Uncertainty in the PSF is due to uncertainty in establishing the ESF via curve fitting of the empirical data. The linearization operation of the data incurs an initial signal uncertainty of 1.25 %. The curve fit also incurs an uncertainty of 2.3 %, which is the RMSE normalized by the range. In order to establish a PSF at the uncertainty extremes, the function is scaled in the positive and negative direction by the combined uncertainty of 2.6 %. From this, new constants a_1, b_1, a_2, and b_2 of Equation (5) are found.

The method described in Section 2.3.4.3 is then used to establish two PSF arrays at both extremes of uncertainty due to the ESF. The images are then deconvolved using the method described in Section 2.3.4.4 with each PSF. The PSF that caused the larger average pixel signal variation from the nominal image is taken as the PSF for uncertainty evaluation, although the change in signal due to either PSF is nearly symmetric. The average deconvolved image produced by the uncertainty of the PSF is then subtracted from the nominal average deconvolved image to establish an uncertainty matrix due to error in the PSF determination.

3.3.7 Deconvolution

The Richardson-Lucy algorithm is among the most robust deconvolution algorithms, but it is an iterative process designed to converge on the most likely reconstructed signal values [24,25]. Conversely, convolution is a destructive forward process that can be done with very little error. Therefore, in order to estimate the uncertainty of the deconvolution, the deconvolved image is convolved and subtracted from the unconvolved image and the magnitude of th signal discrepancy is taken as a conservative estimate of signal uncertainty due to the deconvolution operation at each pixel.

Deconvolution error also occurs due to the saturated region of the image, in which the signal values are no longer proportional to the local radiant flux. In order to reduce the error associated with deconvolution of false signal values, a border of five pixels around the saturated region are discarded. The value of five pixels is chosen because that is the radius within which about 97 % of the PSF volume is contained, and therefore false signal values should have a negligible effect outside of that radius. In future work, signal values may be extrapolated to five pixels within the saturated region to reduce the number of discarded pixels. Or, a further improvement can be implemented by measuring the meltpool at varying shutter speeds to increase the useful dynamic range of measurement, eliminating any saturated signal values.

3.3.8 FPA nonuniformity

As described in Section 3.3.3.1, the FPA nonuniformity is measured after a digital nonuniformity correction and exposure to a uniform source. The pixel average is taken from the 100-image sample, resulting in a calibration image with the average DL of each pixel. The standard deviation across the pixel array is then taken as an evaluation of the nonuniformity across the FPA. The resulting frame standard deviation of the pixel average is expressed as a percentage of the DL. Use of the dynamic range is limited to between 300 DL and 3800 DL, which results in an FPA nonuniformity relative standard uncertainty component of signal of 1.0 %.

3.3.9 Process variability and signal noise

Each image of the central 30 images of the test is deconvolved, and an average of each pixel is taken along with the standard error of the mean of each pixel. The standard error of the mean of each deconvolved pixel is then used as an uncertainty component of the signal due to the physical process variability combined with electronic image noise.

3.3.10 Combined signal uncertainty

The measurement approach requires recording of image data in four steps. The meltpool is recorded with the inline imaging system with the LEDs off, then repeated with the LEDs on. Similarly, the reference mirror is imaged with the LEDs off, then repeated with the LEDs on. With meltpool tests, the frame rate and length of the scan produced image sets containing 80 images. The meltpool requires some "development length" at the initiation of laser melting, and similarly has a cooldown period once the laser power is turned off. Because of these considerations, the first 25 images and last 25 images are not used, and the central 30 images recorded during steady melting are used.

As described in the preceding sections, six sources of uncertainty components in the signal have been identified and quantified. The first uncertainty component is due to the signal linearization operation—it should be noted that this uncertainty is estimated based on a 1.25 % uncertainty in signal values after deconvolution, which inherently assumes that the linearization uncertainty transforms linearly through the deconvolution operation. The second component is incurred by the uncertainty of the stray light and blooming correction operation. The third component is due to the uncertainty in the calculation of the PSF for the deconvolution. The fourth component is based on the discrepancy between the re-convolved deconvolved image compared with the image prior to deconvolution. The fifth component is due to the basic FPA nonuniformity across the field of view. The sixth and final component is the combined effect of signal fluctuation

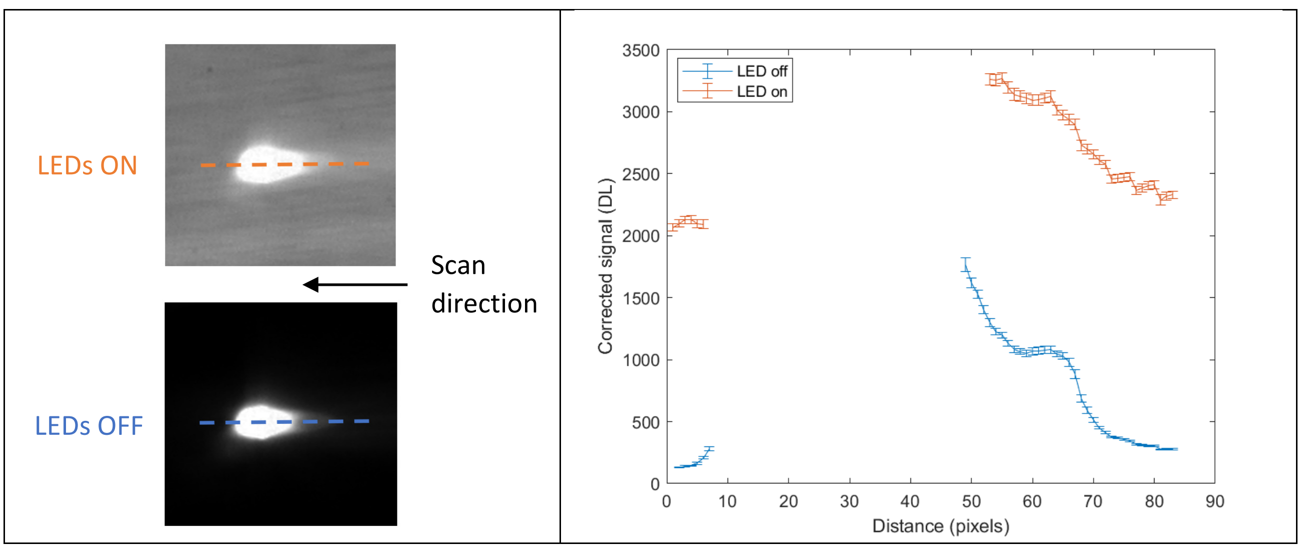

Figure 7. Image data of the meltpool generated with 99.998% Ni with the LEDs on (top left), the LEDs off (lower left), and the associated plot of the corrected signal cross-sections and uncertainties at the location of the dashed lines in the images on the left (right). The data parameters included a laser power of 250 W, scan speed of 1000 mm/s, spot size of 65 µm, image rate of 10000 Hz, and 98.3 µs shutter speed.

due to process variability combined with the electronic noise. Each of the six uncertainty components are calculated independently at each pixel to determine the local uncertainty of the signal of each pixel. The root sum-squares of the six components at each pixel is then evaluated to determine the resulting combined signal uncertainty.

Image data of the reference mirror (with the LEDs on and off) do not require stray light and blooming correction or deconvolution. Therefore, the combined uncertainty of the reference mirror images only has three components: linearization uncertainty, FPA nonuniformity, and pixel noise.

Figure 7 shows meltpool images with the LEDs off, then on, as well as central cross-sectional profiles of the corrected signal and associated uncertainty. The test parameters included a laser power of 250 W, scan speed of 1000 mm/s, spot size of 65 µm, image rate of 10000 Hz, and 98.3 µs shutter speed. The meltpool is generated with 99.998% Ni. As described previously, the signal uncertainty varies with each pixel, but typical uncertainty values are in the approximately 2 %. The solidification plateau is evident from pixel 58 to pixel 64 with the LEDs on and off in Figure 7.

4. EMISSIVITY AND UNCERTAINTY OF A HIGH-PURITY NICKEL MELTPOOL

As stated previously, the test parameters included a laser power of 250 W, scan speed of 1000 mm/s, spot size of 65 µm, image rate of 10000 Hz, and 98.3 µs shutter speed, with the meltpool generated in 99.998% Ni. The resulting emissivity values are shown in Figure 8a and the associated relative standard uncertainty is shown in Figure 8b. Figure 8c shows a central cross-sectional profile of emissivity and uncertainty along the meltpool with nose on the left and tail on the right.

Starting with Figure 8a, it can be observed that the highest emissivity values of more than 0.42 occur near the hotspot. This is likely caused by the depression in the liquid metal generated by a vapor jet emanating from the laser-metal interaction area and the resulting recoil pressure on the liquid surface. The resulting depression in the molten metal becomes a trap for illumination light by multiple reflections, and therefore decreases the local reflectivity, increasing the local emissivity. Intermediate emissivity values of about 0.4 occur in front and to the left and right of the hotspot area in Figure 8. These areas have not been melted by the laser heating, and so the original surface finish of 320 grit sandpaper grinding is maintained. The lowest values of emissivity, below 0.38, occur at the tail of the meltpool where the metal is liquid or recently solidified. These areas that have transitioned to liquid (and/or back to solid) generate more reflective surfaces because surface grinding marks have been eliminated, resulting in lower emissivity. The highest relative standard uncertainty of emissivity also occurs in the tail, which is due in large part to the uncertainty associated with deconvolution in this area of high signal gradients transverse to the meltpool.

The location of the solidification plateau is evident in Figure 7 from pixel 58 to pixel 64, which corresponds to a distance of 350 µm to 385 µm in Figure 8c. The measured value of near-normal spectral emissivity near the melting temperature (1455 °C) of 99.998% Ni is 0.36 with standard relative uncertainty of about 7 %. Published data on similar material at 1491 °C resulted in normal spectral emissivity of about 0.36 at 850 nm [26]. Therefore, under the conditions of comparison, the emissivity measurement approach developed here agrees with published values.

5. CONCLUSIONS AND FUTURE WORK

A unique high temperature reflectometer has been successfully implemented and characterized. The developed reflectometer is, to our best knowledge, the first to use an integrating hemispherical illumination setup, which has proven to be a practical approach. The high-intensity hemispherical illumination (850 nm band) used in this study produces an apparent radiance temperature of the target (with emissivity of 0.5) equal to 1705 °C, which allows for reflectometry of high temperature targets that produce significant self-emission.

This high temperature reflectometer at the NIST AMMT laboratory, with support of the TEMPS optics system and imager, facilitates the measurement of the local spectral directional emissivity, which further facilitates measurement of local surface temperatures of meltpools generated by the laser powder bed fusion process. No performance degradation of the reflectometer is observed due to damage by the high-intensity reflected laser light from the laser-melting process or from contamination by laser-melting process byproducts. Spatial distributions of the emissivity and emissivity uncertainty, of

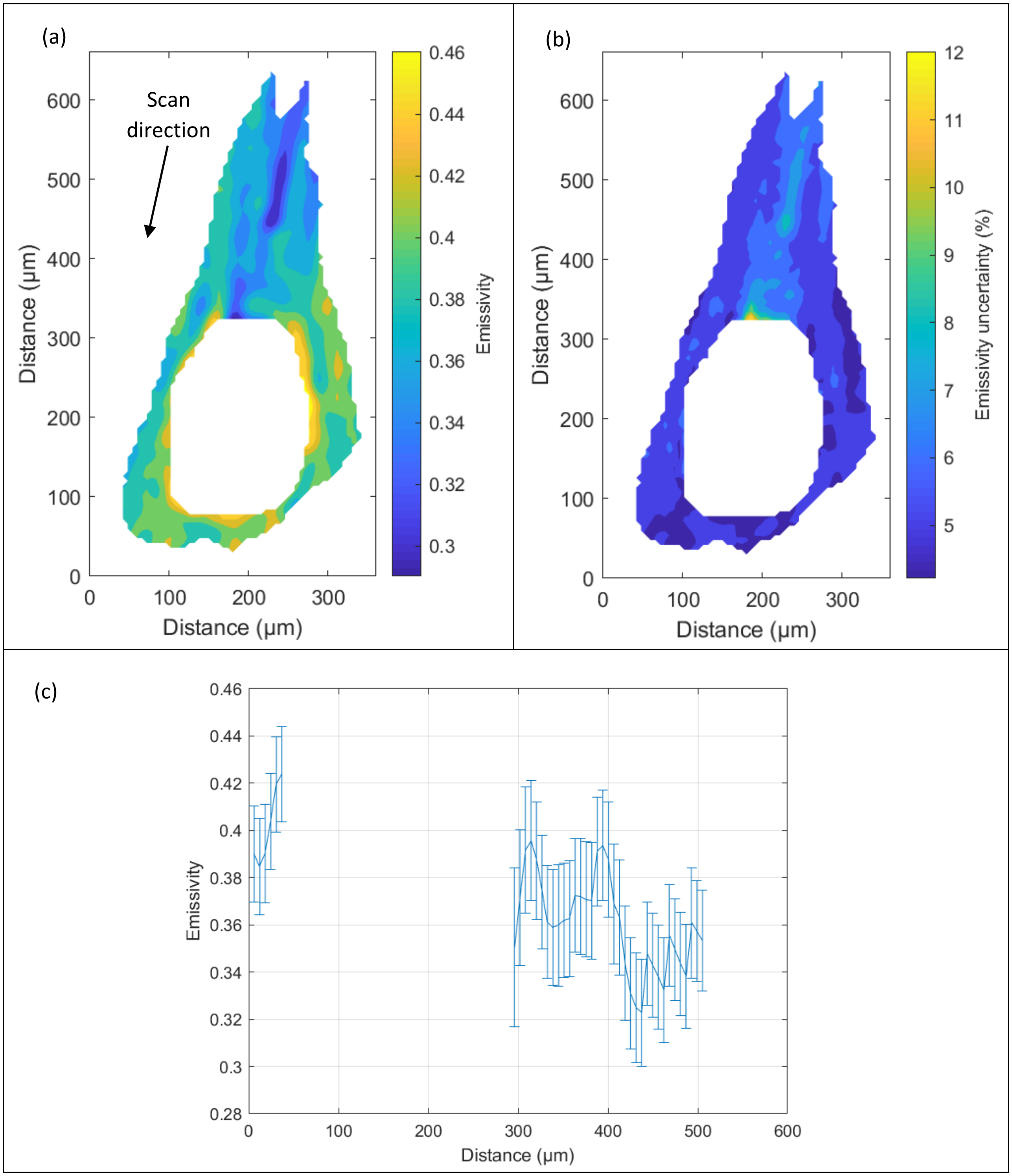

Figure 8. (a) Emissivity map of a meltpool, (b) relative standard uncertainty of the emissivity map, and (c) the central cross-sectional profile of the emissivity and the uncertainty along the meltpool with a nose on the left and a tail on the right. The data parameters included a laser power of 250 W, a scan speed of 1000 mm/s, a spot size of 65 µm, an image rate of 10000 Hz, and a 98.3 µs shutter speed with a 99.998% Ni plate.

a laser-induced meltpool of high-purity nickel, are presented. Some measurement uncertainties were estimated (Type B) in this work, but approaches are identified to better quantify the uncertainty values in the future. The measured emissivity values are found to be in good agreement with literature values at the melting point of high-purity nickel.

Due to the highly non-uniform image scene of a laser-induced meltpool, this investigation focused in part on signal processing, including signal linearization and deconvolution, and the uncertainty induced by those processing operations. Image deconvolution is found to significantly accentuate the solidification plateau of the meltpool due to the high local signal gradients, although the effect generally cancels out in the emissivity measurement equation due to an approximately equivalent effect of deconvolution with images taken with and without hemispherical illumination. Nevertheless, the current results indicate that signal processing, including deconvolution, has important ramifications for the measurement of thermodynamic surface temperatures. Approaches for estimating uncertainties associated with stray light and blooming correction, as well as deconvolution have been identified and implemented in this work.

Several hardware improvements may be implemented in the future to improve the utility of the emissivity measurement approach described here. The current reflectometer configuration uses continuous illumination by high intensity LEDs at 850 nm. The LEDs are modularized and can be changed if necessary, for measurement in other spectral bands. LEDs with shorter wavelengths will enable measurement of equivalent radiance temperatures of the probing light up to 2650 °C (for a 405 nm band illumination with a target emissivity of 0.5). Future hardware improvements also include the use of pulsed narrow band sources to increase the temperature range further, use of a thin bottom to increase the angular range of the illumination, adding the ability to translate the reflectometer, as well improvement of the shield gas arrangement to be able to work with powders. Future research also includes more detailed quantification of the port loss effects and other sources of uncertainty, especially if lower levels of uncertainty are needed. Finally, quantification of the measurement bias and uncertainty induced by laser-melting byproduct effects, such as scatter and diffraction of probing and/or reflected light by the metal vapor and condensate, will be a topic of future research.

ACKNOWLEDGEMENTS

The authors wish to thank Vladimir Khromchenko of NIST Physical Measurement Laboratory (PML) and Daniel Cardenas-Garcia of the National Metrology Center of Mexico for their work in characterizing the reflectometer. The authors also wish to thank Steve Grantham of NIST PML for his work on design and implementation of the reflectometer and LED power control. The authors further wish to thank Ivan Zhirnov formerly of NIST PML for his work in evaluation of sample/mirror alignment effects and taking of experimental data. The authors finally wish to than Brandon Lane of NIST Engineering Laboratory for his technical review of this content.

REFERENCES

[1] Herzog, D., Seyda, V., Wycisk, E. and Emmelmann, C., “Additive manufacturing of metals,” Acta Mater. 117, 371–392 (2016).
[2] Mitchell, J. A., Ivanoff, T. A., Dagel, D., Madison, J. D. and Jared, B., “Linking pyrometry to porosity in additively manufactured metals,” Addit. Manuf. 31, 100946 (2020).
[3] Hanssen, L. M., Mekhontsev, S. N. and Khromchenko, V. B., “Infrared spectral emissivity characterization facility at NIST,” Thermosense XXVI 5405, 1–12, International Society for Optics and Photonics (2004).
[4] Lane, B., Moylan, S., Whitenton, E. P. and Ma, L., “Thermographic measurements of the commercial laser powder bed fusion process at NIST,” Rapid Prototyp. J. (2016).
[5] Reijonen, J., Revuelta, A., Riipinen, T., Ruusuvuori, K. and Puukko, P., “On the effect of shielding gas flow on porosity and melt pool geometry in laser powder bed fusion additive manufacturing,” Addit. Manuf. 32, 101030 (2020).
[6] Lane, B., Mekhontsev, S., Grantham, S., Vlasea, M., Whiting, J., Yeung, H., Fox, J., Zarobila, C., Neira, J. and McGlauflin, M., “Design, developments, and results from the NIST additive manufacturing metrology testbed (AMMT),” Solid Free. Fabr. Symp., 1145–1160 (2016).
[7] Yeung, H., Neira, J., Lane, B., Fox, J. and Lopez, F., “Laser path planning and power control strategies for powder bed fusion systems,” Solid Free. Fabr. Symp., 113–127 (2016).

[8] Shiraiwa, H. and Sano, H., “Reference light source device used for calibration of spectral luminance meter and calibration method using same,” US10330530B2 (2019).
[9] Ahn, J., He, E., Chen, L., Dear, J. and Davies, C., “The effect of Ar and He shielding gas on fibre laser weld shape and microstructure in AA 2024-T3,” J. Manuf. Process. 29, 62–73 (2017).
[10] Malekipour, E. and El-Mounayri, H., “Common defects and contributing parameters in powder bed fusion AM process and their classification for online monitoring and control: a review,” Int. J. Adv. Manuf. Technol. 95(1–4), 527–550 (2018).
[11] Ladewig, A., Schlick, G., Fisser, M., Schulze, V. and Glatzel, U., “Influence of the shielding gas flow on the removal of process by-products in the selective laser melting process,” Addit. Manuf. 10, 1–9 (2016).
[12] Grantham, S., Lane, B., Neira, J., Mekhontsev, S., Vlasea, M. and Hanssen, L., “Optical design and initial results from NIST’s AMMT/TEMPS facility,” Laser 3D Manuf. III 9738, 97380S, International Society for Optics and Photonics (2016).
[13] Lane, B. and Whitenton, E., “Calibration and measurement procedures for a high magnification thermal camera,” Rep. No NISTIR8098, Natl. Inst. Stand. Technol. (2015).
[14] “ISO 12233:2017 Photography — Electronic still picture imaging — Resolution and spatial frequency responses.”
[15] Richardson, W. H., “Bayesian-Based Iterative Method of Image Restoration,” JOSA 62(1), 55–59 (1972).
[16] Lucy, L. B., “An iterative technique for the rectification of observed distributions,” Astron. J. 79, 745 (1974).
[17] BIPM, IEC, IFCC, ILAC, ISO, IUPAC, IUPAP and OIML., “Guide to the Expression of Uncertainty in Measurement,” JCGM 100:2008, (2008).
[18] Barnes, P. Y., Parr, A. C. and Early, E. A., “NIST Measurement Services: Spectral Reflectance,” NIST Spec. Pub. 250-48, Natl. Inst. Stand. Technol. (1998).
[19] Hanssen, L. M., “Effects of non-Lambertian surfaces on integrating sphere measurements,” Appl. Opt. 35(19), 3597–3606 (1996).
[20] Hanssen, L. M. and Snail, K. A., [Integrating spheres for mid-and near-infrared reflection spectroscopy], John Wiley & Sons, Ltd New York (2002).
[21] “Avian-B White Reflectance Coating.”, Avian Technol.
[22] LED Engin., “850nm Infrared LED Emitter LZ4-00R408” (2018).
[23] Hanssen, L., “Integrating-sphere system and method for absolute measurement of transmittance, reflectance, and absorptance of specular samples,” Appl. Opt. 40(19), 3196–3204 (2001).
[24] Fish, D. A., Brinicombe, A. M., Pike, E. R. and Walker, J. G., “Blind deconvolution by means of the Richardson–Lucy algorithm,” JOSA A 12(1), 58–65 (1995).
[25] Gladysz, S. and Gallé, R. B., “Comparison of image restoration algorithms in the context of horizontal-path imaging,” Infrared Imaging Syst. Des. Anal. Model. Test. XXIII 8355, 83550X, International Society for Optics and Photonics (2012).
[26] Krishnan, S., Yugawa, K. J. and Nordine, P. C., “Optical properties of liquid nickel and iron,” Phys. Rev. B 55(13), 8201–8206 (1997).